

Optimal Pt–Au Alloying for Efficient and Stable Oxygen Reduction Reaction Catalysts

Xianxian Xie, Valentín Briega-Martos, Riccardo Farris, Milan Dopita, Mykhailo Vorokhta, Tomáš Skála, Iva Matolínová, Konstantin M. Neyman, Serhiy Cherevko, and Ivan Khalakhan*



Cite This: *ACS Appl. Mater. Interfaces* 2023, 15, 1192–1200



Read Online

ACCESS |



Metrics & More



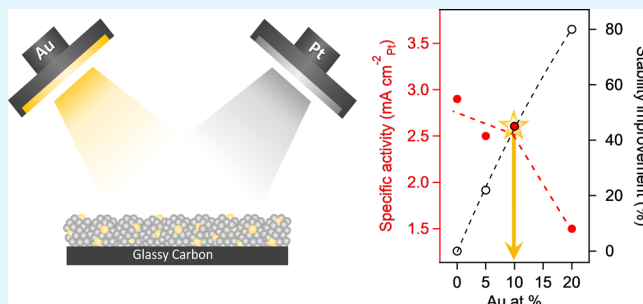
Article Recommendations



Supporting Information

ABSTRACT: Stabilization of cathode catalysts in hydrogen-fueled proton-exchange membrane fuel cells (PEMFCs) is paramount to their widespread commercialization. Targeting that aim, Pt–Au alloy catalysts with various compositions (Pt₉₅Au₅, Pt₉₀Au₁₀, and Pt₈₀Au₂₀) prepared by magnetron sputtering were investigated. The promising stability improvement of the Pt–Au catalyst, manifested in suppressed platinum dissolution with increasing Au content, was documented over an extended potential range up to 1.5 V_{RHE}. On the other hand, at elevated concentrations, Au showed a detrimental effect on oxygen reduction reaction activity. A systematic study involving complementary characterization techniques, electrochemistry, and Monte Carlo simulations based on density functional theory data enabled us to gain a comprehensive understanding of the composition–activity–stability relationship to find optimal Pt–Au alloying for maintaining the activity of platinum and improving its resistance to dissolution. According to the results, Pt–Au alloy with 10% gold represent the most promising composition retaining the activity of monometallic Pt while suppressing Pt dissolution by 50% at the upper potential limit of 1.2 V_{RHE} and by 20% at devastating 1.5 V_{RHE}.

KEYWORDS: fuel cells, oxygen reduction reaction, platinum dissolution, Pt–Au alloy, activity–stability relationship



INTRODUCTION

According to the recently announced Green Deal, hydrogen-fueled proton-exchange membrane fuel cells (PEMFCs) are expected to be one of the pillars of a future sustainable green-energy system.¹ Alongside water electrolyzers, fuel cells are considered to smooth out the intermittency of electricity produced from renewable sources. To date, the main limitations hindering the vast commercialization of such fuel cells reside on its cathode side, where a sluggish oxygen reduction reaction (ORR) takes place.² Because of that, PEMFC cathodes require a large amount of expensive platinum catalysts, which moreover operate under aggressive corrosive environments. Therefore, recent research efforts have been focused on improving the cost efficiency and/or stability of ORR catalysts.

While most studies focus on increasing ORR catalyst cost-efficiency, significantly less attention has been devoted to improving its stability. Even though platinum is a noble metal, it is not entirely resistant to degradation under a hostile electrochemical environment of the cathode. Relatively high potentials in combination with an acidic environment cause Pt dissolution and carbon support corrosion, which further trigger secondary degradation processes, such as detachment of Pt nanoparticles from the support, particle coalescence, and the so-called electrochemical Ostwald ripening.^{3–7} Additionally,

dissolved Pt was found to recrystallize in the polymer membrane and lower its proton conductivity.⁸ Moreover, all the above processes are enhanced at higher operating potentials, which are difficult to mitigate at the start/stop operational regimes of PEMFC.⁹ This leads to an irreversible detrimental effect on performance during fuel cell operation owing to continuous reduction of the available platinum catalyst active sites and proton conductivity of the Nafion membrane.

Studies of the abovementioned degradation mechanisms of ORR catalysts and their underlying principles pointed out that the inhibition of Pt dissolution is crucial for suppressing their deterioration. Platinum dissolution in PEMFCs is governed by their successive oxidation and reduction due to the transient nature of PEMFC devices. The development of *in situ* techniques based on inductively coupled plasma mass spectrometry (ICP-MS) allowed to elucidate fundamental aspects of platinum dissolution and to establish relationships

Received: October 17, 2022

Accepted: December 15, 2022

Published: December 28, 2022



between potential-dependent oxide formation in various environments.^{10–15} On the one hand, Pt dissolution takes place in the initial steps of surface oxidation during transient experiments, involving a change in the oxidation state of the metal and/or oxide/hydroxide stoichiometry. This is the so-called “anodic dissolution”. On the other hand, during the reduction of the metal oxides, reverse processes occur with the formation of an unstable oxide and its partial dissolution. This is typically called “cathodic dissolution”. The dissolved quantities depend on the amount of pre-formed oxide and the rate of re-deposition of dissolved species.¹⁶ All these factors should be considered when designing an ORR catalyst to effectively address its durability.

Alongside other strategies, such as catalyst shape control¹⁷ and its surface coating by a thin protective layer,^{18,19} incorporating specific elements into platinum has recently been proven favorable to alleviate its dissolution. Among alloying elements, gold has been reported as one of the most promising choices so far due to its inertness.^{20–24} Back in 2007, Zhang et al. showed that decorating Pt nanoparticles with Au clusters suppresses Pt dissolution under PEMFC working conditions.²³ No obvious performance degradation was observed even after 30,000 accelerated degradation test (ADT) cycles. *In situ* X-ray absorption near-edge spectroscopy and voltammetry revealed that the Au clusters confer stability by raising the Pt oxidation potential. It was later confirmed in the case of a Pt submonolayer on Au using a scanning flow cell (SFC) coupled to ICP-MS. A direct comparison of the dissolution rates pointed out that Pt dissolution is suppressed in the presence of an Au underlayer.²¹ More recently, it was shown that, besides the early reported selective healing of the surface low-coordinated Pt sites, an Au underlayer also promotes the ordering of Pt surface atoms toward a more stable (111) structure, hence suppressing Pt dissolution.²² These findings were further demonstrated on a nanoparticle catalyst consisting of a Au core surrounded by a 1 nm thick mixed Pt–Au shell with a Pt-rich surface. Such catalyst exhibited 30 times greater durability than Pt/C over an extended potential range up to 1.2 V. Similarly, Takahashi et al. showed that the Au atoms located in coordinatively unsaturated sites, e.g., at corner or edge ones of Pt nanoparticles, can improve the durability of ORR catalysts.²⁴ The above research proved that mixing with gold not only increases the oxidation potential of platinum but also protects its low-coordinated surface sites. Although, in general, gold fails to effectively address the cost issue, such a Pt–Au composite is undoubtedly an attractive solution for improving the stability of Pt against dissolution, thereby opening up prospects for the development of long-lasting ORR catalysts. The challenges and opportunities of the Pt–Au system for the ORR are summarized in a recent perspective paper.²⁵

Despite the advantages and great potential of Pt–Au alloys, a significant drawback exists. The gold itself is not active for the ORR. Moreover, its alloying with platinum makes it unfavorable for ORR geometrical modifications.²⁶ The effectiveness of Pt–Au for both activity and durability thus strongly depends on the alloy structure as well as the compositional profile and, therefore, should be balanced through precise catalyst engineering.

Herein, we report a systematic study of Pt–Au bimetallic alloys with different compositions prepared using a magnetron sputtering technique. Powerful surface characterization techniques, electrochemistry, and Monte Carlo simulations relying

on density functional results were applied to gain a comprehensive understanding of the composition–activity–stability relationship in order to find optimal Pt–Au alloying to effectively address both requirements: maintain the ORR activity and improve Pt resistance to dealloying.

EXPERIMENTAL SECTION

Sample Preparation. Pt–Au alloys were deposited on glassy carbon (GC) substrates (Alfa Aesar) by magnetron co-sputtering using two circular TORUS magnetrons (Lesker) placed under the angle of 45° to the substrate and two targets: 2” Pt (99.99 % Safina) and 2” Au (99.99% Kurt J. Lesker). The sputtering was carried out in 0.5 Pa of an Ar atmosphere in DC mode by applying 90 W to Pt and 2, 5, and 10 W to the Au target, resulting in the deposition of Pt₉₅Au₅, Pt₉₀Au₁₀, and Pt₈₀Au₂₀ layers, respectively. The reference monometallic Pt and Au layers were deposited using corresponding single-metal targets. The nominal thickness of all the investigated catalytic layers was kept constant at about 10 nm.

Sample Characterization. Atomic Force Microscopy (AFM). The morphology of catalysts was examined using a MultiMode 8 AFM (Bruker) in tapping mode under ambient conditions. SCANASYST-AIR probes (Bruker) with a nominal tip radius of 2 nm were used. Image processing was carried out using the NanoScope 1.9 software.

Energy-Dispersive X-ray Spectroscopy. The bulk composition of the as-deposited Pt–Au samples was determined by energy-dispersive X-ray spectroscopy (EDX) using an XFlash detector (Bruker) integrated into the Mira 3 (Tescan) scanning electron microscope (SEM) operating at 20 keV electron beam energy.

Photoelectron Spectroscopy. The high-resolution synchrotron radiation photoelectron spectroscopy (SRPES) measurements were performed at the Materials Science Beamline at the Elettra synchrotron light source in Trieste, Italy. The beamline uses a plane grating monochromator, providing narrow-band synchrotron light in the energy range of 21–1000 eV. The end station consists of a main ultra-high vacuum (UHV) chamber (base pressure 2×10^{-8} Pa) equipped with a Phoibos 150 electron energy analyzer (Specs). The 180 eV excitation energy was used to measure Pt 4f and Au 4f core-levels in order to obtain the highest surface sensitivity. Sample cleaning was performed through its exposure to the hydrogen atmosphere (5 mbar, room temperature) with further mild Ar⁺ ion bombardment (1000 eV for 5 min). Conventional XPS was performed in the same setup using an Al K α X-ray source with fixed 1486.6 eV photon energy.

X-ray Diffraction. The X-ray diffraction (XRD) measurements were performed using a Rigaku SmartLab diffractometer equipped with a 9 kW rotating anode X-ray source (Cu K α radiation, $\lambda = 0.15418$ nm), a parabolic multilayer mirror in the primary beam, a set of axial divergence eliminating Soller slits with acceptance 5° in both incident and diffracted beam, and a HighPix-3000 2D hybrid pixel single-photon counting detector. The XRD measurements were done in the parallel beam—glancing angle X-ray diffraction geometry (GAXRD) with a parallel beam Soller slit collimator (acceptance 0.5°) in the diffracted beam. The constant angle of the incidence beam of 0.6° was used for the measurements.

Rotating Disc Electrode. Electrochemical measurements were performed using a rotating disk electrode (RDE) setup (Pine Research) connected to an SP-150 potentiostat (Bio-Logic). A typical three-electrode configuration was used with a catalyst deposited onto GC (Pine Research, 5 mm diameter, 0.196 cm² surface area) as a working electrode, platinum wire as a counter electrode (99.99%, Pine Research), and leak-free Ag/AgCl in saturated KCl as a reference electrode (Monokrystaly s.r.o.). All measurements were performed at room temperature. All potentials in this paper refer to a reversible hydrogen electrode (RHE). The cyclic voltammograms (CVs) were recorded in N₂-saturated 0.1 M HClO₄ electrolyte solution at 200 mV s⁻¹ sweep rate.

To obtain CO stripping voltammograms, 0.1 M HClO₄ electrolyte solution was first saturated with CO gas while keeping the cell

potential at 0.15 V_{RHE} . Then, the solution was purged with N_2 gas for 20 min to remove CO not bonded to platinum. After purging, linear sweep voltammetry was conducted from 0.05 to 1.5 V_{RHE} with a scan rate of 20 mV s^{-1} .

The ORR activity of the catalysts was evaluated using linear sweep voltammetry (LSV) in an O_2 -saturated 0.1 M $HClO_4$ electrolyte at 20 mV s^{-1} scan rate and 1600 rpm rotation speed.

Electrochemical Scanning Flow Cells with ICP-MS. Electrochemical transient dissolution of ^{195}Pt and ^{197}Au was monitored employing previously described SFC-ICP-MS systems.^{13,27} Saturated Ag/AgCl (Metrohm) and a GC rod (HTW Sigradur G) were used as reference and counter electrodes, respectively. The working electrode contact area was approximately 1.1 mm^2 . Freshly prepared 0.1 M $HClO_4$ from 70% perchloric acid (Suprapur, Merck) and ultrapure water (Milli-Q IQ 7000, Merck) was used as an electrolyte with a flow rate from 197 to 205 $\mu\text{L min}^{-1}$ with continuous argon purging. The flow rate varied as pump tubing aged. Dissolution was monitored on a NexION 300 (Perkin Elmer) ICP-MS via calibration from Pt and Au solutions (Certipur, Merck), while 10 $\mu\text{g L}^{-1}$ ^{187}Re were used as internal standards for ^{195}Pt and ^{197}Au , respectively. Total quantities of dissolution were obtained via integration of the transient dissolution profiles.

Computational Modeling. The lowest-energy arrangement of different metal atoms in bimetallic nanoparticles of a given structure and composition (chemical ordering) can be efficiently determined computationally using a Topological (TOP) method^{28,29} that combines density functional theory (DFT) calculations of selected orderings with Monte Carlo (MC) exploration of a huge configurational space of the possible orderings. The TOP method has been recently applied to calculate chemical orderings in Pt–Au nanoparticles with Au content ≥ 25 at.%.³⁰ Using the TOP equations obtained there, ca. 4 nm large octahedral-like $\text{Pt}_{1463-x}\text{Au}_x$ particles with the fcc-structure and increasing Au content were modeled: $\text{Pt}_{1434}\text{Au}_{29}$, $\text{Pt}_{1406}\text{Au}_{57}$, $\text{Pt}_{1349}\text{Au}_{114}$, $\text{Pt}_{1291}\text{Au}_{172}$. The outer atomic layer of these particles consists of 24 corner, 108 edge, and 440 (111) facet atoms. Thus, the chosen stoichiometries correspond to 5, 10, 20, and 30 at.% Au in the surface layer to represent the experimentally investigated compositions. The most stable chemical orderings, revealing the predicted arrangement of surface Au and Pt atoms at 300 K, were obtained from the MC simulations as detailed elsewhere.³⁰ DFT calculations of the relative stability of the corner, edge, and surface terrace Pt atoms were performed for the truncated-octahedral Pt_{405} particle following the protocol presented in ref 31.

Although the employed computational models are idealized in terms of regular and well-organized arrangements of atoms, this idealization is not expected to critically affect the representation of the main reactivity features of the catalysts prepared by magnetron sputtering exhibiting quite irregular arrangements.

RESULTS AND DISCUSSION

Three Pt–Au layers with different compositions were prepared, from now on referred to as PtAu5, PtAu10, and PtAu20, corresponding to $\text{Pt}_{95}\text{Au}_5$, $\text{Pt}_{90}\text{Au}_{10}$, and $\text{Pt}_{80}\text{Au}_{20}$. The AFM images of all investigated samples are depicted in Figure 1a. The morphology reveals homogeneously distributed grains with high-angle boundaries in close proximity to each other, which is typical for layers deposited by magnetron sputtering. Statistical parameters such as root mean square roughness (R_q , represents vertical roughness of the surface) and the correlation length (ξ , describes the lateral roughness of the surface and is associated with the grain size) were extracted from the corresponding images to analyze morphology in more detail.³² Both R_q and ξ remain similar for all samples ($\xi = 4.5 \pm 0.1$ nm, $R_q = 0.5 \pm 0.01$ nm), evidencing essentially identical morphology regardless of the composition, avoiding thus its possible influence on the ORR activity. It should also be noted that because of the convolution of the AFM tip and the surface,

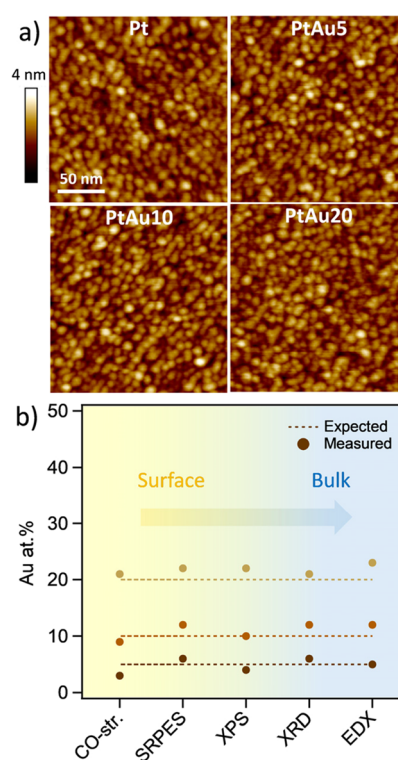


Figure 1. (a) AFM images of the as-deposited Pt–Au alloy and pure Pt catalysts; (b) comparison of the Pt–Au alloy composition calculated using CO stripping (Figure 3b), SRPES (Figure 2c,d), XPS (Figure S1b), XRD (Figure 2a), and EDX (Figure S1a) techniques. Dashed lines present nominal compositions.

these values should not be taken into account as absolute values.

The composition of as-deposited samples was verified by multiple surface (CO stripping, SRPES, XPS) and bulk (XRD, EDX) sensitive techniques. All nicely correlate with the given Au concentrations in the alloy with only slight deviations, further confirming the uniform composition gradient, as summarized in Figure 1b.

The XRD patterns acquired from Pt–Au layers are shown in Figure 2a together with pure Pt to facilitate the comparison. All reflections correspond to a single phase of the face-centered cubic (fcc) (space group $Fm\bar{3}m$, No. 225) structure. A closer inspection of the XRD patterns reveals a continuous shift of all diffraction peaks toward lower angles with respect to the pure Pt with increasing Au content, as highlighted for the Pt(111) line in the inset of Figure 2a. Such behavior implies the formation of tensile strain originating from the larger Au atom. Indeed, the lattice constant quantified from the corresponding patterns and plotted in Figure 2b linearly increases with Au concentration following Vegard's law (The lattice parameters for bulk Pt and Au are also included for comparison). These results confirm that despite immiscibility of Pt and Au, Pt–Au catalysts prepared by magnetron sputtering display alloy properties, which is in line with previous studies on a nanoscale Pt–Au system prepared by other methods.^{26,33,34} The lattice expansion with respect to that of pure Pt calculated from XRD is 0.25, 0.44, and 0.82% for PtAu5, PtAu10, and PtAu20, respectively.

The samples were further analyzed using surface-sensitive SRPES in order to evaluate changes in the electronic structure of Pt and Au caused by their alloying. All samples were cleaned

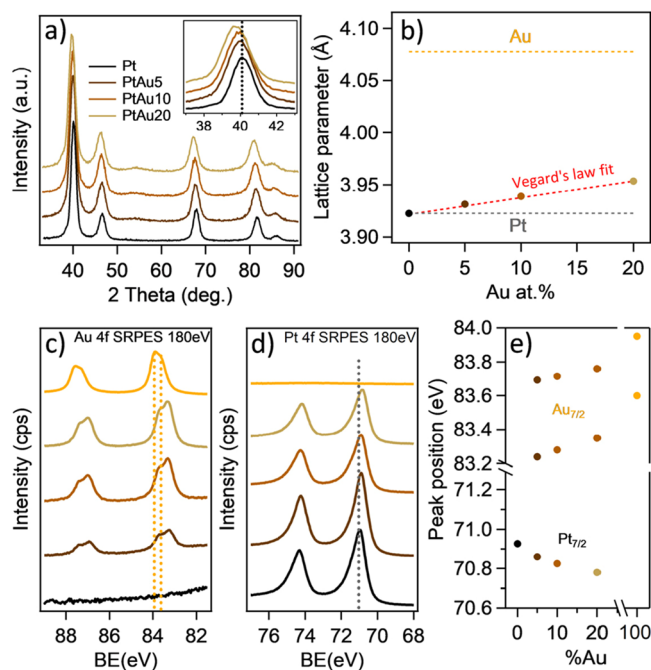


Figure 2. (a) XRD patterns of the as-deposited Pt–Au alloy catalysts (inset highlights the 111 peak) and (b) evolution of corresponding lattice parameters; (c) SRPES Au 4f and (d) SRPES Pt 4f spectra acquired for as-deposited Pt–Au alloy catalysts (dashed lines highlight the position of the $4f_{7/2}$ peak for monometallic Pt or Au); (e) evolution of Au $4f_{7/2}$ and Pt $4f_{7/2}$ BEs with varying Au contents extracted from the spectra shown in (c) and (d).

prior to measurements according to the procedure described in the experimental part. The photoelectron Au 4f and Pt 4f spectra recorded at 180 eV photon energy, which allows collecting information from the top 2–3 monolayers of the alloy, are shown in Figure 2c,d. The high-resolution Pt 4f spectrum of pure platinum (bottom spectrum in Figure 2d) is represented by a single doublet with a significantly asymmetric shape at 70.95–74.25 eV, typical for metallic platinum.^{35,36} In

contrast, the Au 4f core level of monometallic gold (upper spectrum in Figure 2c) reveals the existence of two components at 83.95–87.69 and 83.6–87.36 eV, corresponding to the bulk (subsurface) and surface gold atoms.^{37,38} The shape of the SRPES spectra persists for the whole range of alloy composition. Nevertheless, the continuous shift of both Pt 4f and Au 4f regions (highlighted as the $4f_{7/2}$ peak position for Pt and Au components in Figure 2e) can be observed relative to the pure metals, evidencing changes in the electronic structure of both elements due to the higher electronegativity of Au.^{30,39,40} Since, in our case, lower amounts of gold are dissolved in the platinum host, Pt 4f is less affected by alloying than Au 4f. The quantified Pt 4f core-level shifts compared to the peak position for monometallic Pt are -0.07 , -0.10 , and -0.15 eV for PtAu5, PtAu10, and PtAu20, respectively. Based on the above XRD and SRPES data, precise adjustment of the amount of gold in Pt–Au alloy allows accurate tuning of platinum geometrical and electronic structure.

An electrochemical study was further performed. CVs acquired in N_2 -saturated 0.1 M $HClO_4$ for all investigated samples are displayed in Figure 3a and compared with the CVs for monometallic platinum and gold (note that the upper potential of 1.6 V_{RHE} was chosen to observe Au oxidation/reduction couple). The CVs display typical electrochemical signatures of both polycrystalline platinum and gold. It can be qualitatively observed that as the Au amount increases, the intensity of the CV peaks associated with surface Pt decreases, while the intensity related to surface Au increases. A closer inspection of CVs reveals that the peak potential value for gold oxide reduction shifts significantly to higher potentials with Au increase, whereas platinum oxide reduction peak shows only negligible potential shift to lower potentials, implying slightly higher platinum affinity to oxygen, which is in line with the literature.⁴¹

Figure 3b compares the CO stripping voltammograms acquired in CO-saturated 0.1 M $HClO_4$ for all investigated samples. The CO stripping peak centers at 0.68 V_{RHE} for pristine Pt and then continuously shifts toward higher potentials with addition and further increase of Au, reaching

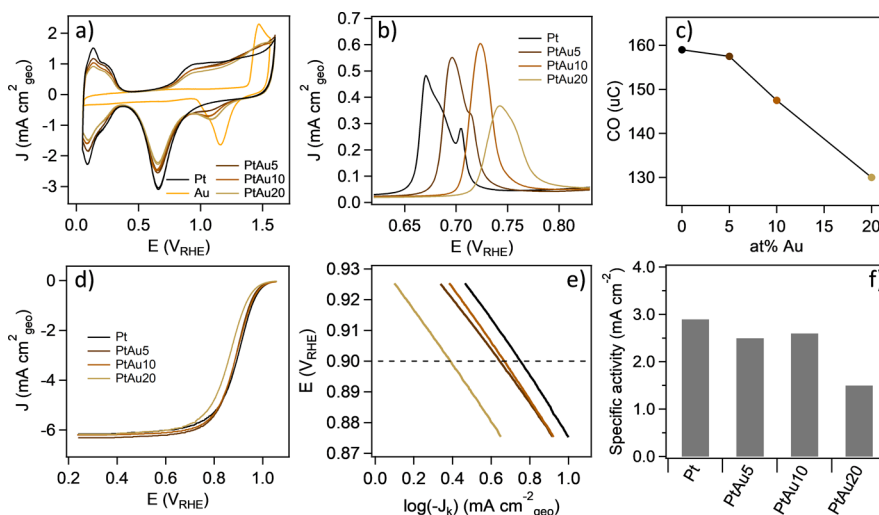


Figure 3. (a) CVs recorded in N_2 -saturated 0.1 M $HClO_4$ and (b) CO-stripping voltammograms recorded in CO-saturated 0.1 M $HClO_4$ of the as-deposited Pt–Au alloy catalysts; (c) evolution of CO charge calculated from the voltammograms shown in b); (d) ORR polarization curves of the as-deposited Pt–Au alloy catalysts recorded in O_2 -saturated 0.1 M $HClO_4$ at 1600 rpm rotation speed; (e) corresponding Tafel plots; (f) specific activity values at 0.9 V_{RHE} .

0.74 V_{RHE} for the PtAu20 sample. This implies an increased CO binding energy induced by Pt modification and correlates well with previous studies on Pt/Au systems.^{42,43} The CO oxidation charge evaluated by integrating the corresponding CO stripping peaks and, as shown in Figure 3c, decreases with increasing Au content, indicating a lower electrochemically active surface area (ECSA) caused by the presence of Au atoms on the surface. The outermost surface compositions calculated using CO desorption charge, considering that it is 100% for pure platinum, are Pt₉₇Au₃, Pt₉₁Au₉, and Pt₇₉Au₂₁, which agrees with that measured by SRPES, XPS XRD, and EDX (see Figure 1b).

The ORR activity of the catalysts was examined in an O₂-saturated 0.1 M HClO₄ electrolyte. The polarization curves for PtAu5 and PtAu10 samples in Figure 3d are very similar to the one for pure Pt showing comparable half-wave potential ($E_{1/2} \sim 0.9 V_{\text{RHE}}$). This indicates that 5 and 10% of Au have minimal effect on the ORR activity. On the contrary, the PtAu20 sample shows markedly lower activity manifesting in the negative shift of the half-wave potential by about 40 mV ($E_{1/2} = 0.86 V_{\text{RHE}}$). To get a deeper insight into the ORR activity, a detailed kinetic analysis was carried out (see Electronic Supplementary Material for details). Tafel plots derived from the ORR polarization curves were analyzed in the vicinity of 0.9 V and shown in Figure 3e (Tafel plots in the whole potential range are shown in Figure S2a). As shown in Figure S2b, Tafel slopes of $\sim 90 \text{ mV dec}^{-1}$ were fitted for all Pt–Au catalysts at the high potential region from 0.93 to 0.87 V, which is in close agreement with that of monometallic Pt reported previously,^{44,45} indicating a similar ORR pathway with the pure Pt surface at the high potential region. The specific activity (SA, which is defined as the kinetic current density, J_k , normalized by the Pt area obtained by the CO stripping measurements) values at 0.9 V_{RHE} in turn are shown in Figure 3f. The SA remains within 2.6–2.9 $\text{mA cm}^2_{\text{Pt}}$ for PtAu5 and PtAu10, which is typical for polycrystalline Pt based on previous reports^{46,47} while the PtAu20 sample shows markedly lower activity manifesting in a nearly double decrease of SA. The above results clearly evidence a threshold in Au concentration within 10–20 at.% below which Pt retains its activity.

Similar findings have been made by other researchers for Au/Pt model systems. For example, in a recent study, Lopes et al. reported the optimal coverage of up to 0.2 ML of Au on Pt(111), where a negligible impact on the ORR rate was observed and related to the fact that Au atoms are preferentially placed at Pt(111) step-edge sites.²² However, increasing the Au coverage above that value resulted in a measurable decrease in the ORR, which, in turn, coincided with Au spillover on Pt terraces. Takahashi et al. found that with the increase in the Au content deposited on Pt nanoparticles, the ECSA of the Au_x/Pt₁₀₀ ($x = 0\text{--}42$) gradually decreased. Nevertheless, the specific ORR activity of the samples revealed a volcano-type trend, where Au₂₈/Pt₁₀₀ showed the highest SA among all the investigated samples.²⁴ Lack of ORR inhibition in the case of Au clusters decorating Pt nanoparticles despite blockage of approximately 30% of the Pt sites was concluded by Zhang et al.²³

The above experimental observations on Au/Pt model systems directly relating the content of Au on the surface of Pt with its activity are supported by the results of our computational experiments on Pt–Au nanoparticles summarized in Figure 4. Note that these simplified simulations do not

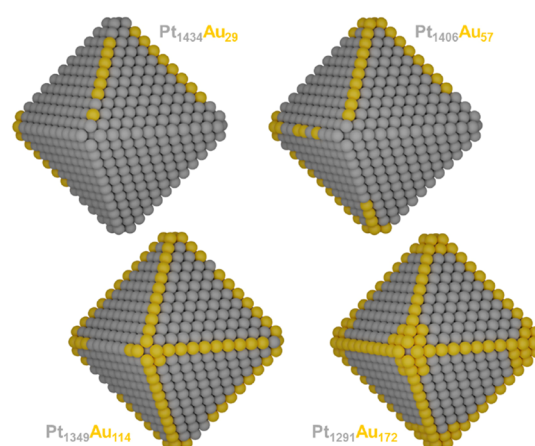


Figure 4. Equilibrium chemical orderings of ca. 4 nm large Pt–Au particles with Au content in the outer atomic shell of 5, 10, 20, and 30 at.% calculated at temperature 300 K: Pt₁₄₃₄Au₂₉ (4,25,0), Pt₁₄₀₆Au₅₇ (12,45,0), Pt₁₃₄₉Au₁₁₄ (23,89,2), and Pt₁₂₉₁Au₁₇₂ (24,108,40). In parentheses, the numbers of Au atoms in the corner, edge, and (111) surface terrace positions, respectively, are shown. Atom color coding: Pt–gray; Au–yellow.

reveal bulk Au atoms in the equilibrium chemical orderings of Au/Pt model particles. There, the lowest-energy topologies (atomic orderings) of 1463 atomic particles containing the increasing number of Au atoms on the surface (at 5, 10, 20, and 30% of the total atoms in the monoatomic skin) are shown. DFT calculations of Pt–Au nanoparticles^{30,31} reveal a strong energy driving force for Au atoms to stay in the outer monoatomic shell of particles, preferentially in the corner and edge positions with the lowest coordination, where each Au atom is $\geq 0.5 \text{ eV}$ more stable than inside the particle; displacement of an inner Au atom to a (111) terrace position is also notably favorable, by 0.3–0.4 eV.

Accordingly (see Figure 4), the calculated equilibrium chemical ordering of Pt₁₄₃₄Au₂₉ particles with 5% of Au atoms in the skin features their locations exclusively in the corner (4 of 24) and edge (25 of 108) positions. Pt₁₄₀₆Au₅₇ particles with Au surface content increased to 10% feature low-coordinated Pt atoms in the corner and edge sites, but still, there was no decrease in the number of active Pt atoms in (111) nanofacets. Further increase of Au content, Pt₁₃₄₉Au₁₁₄ with 20% of Au, already results in the appearance of first Au atoms in the (111) terraces—the onset of detrimental effects for ORR activity by decreasing the number of active sites. At 30% of surface Au, Pt₁₂₉₁Au₁₇₂ model, there are no corner or edge Pt atoms at all and this particle exposes 40 Pt atoms less in (111) terrace sites than the other three models, i.e., notably less active surface Pt atoms mediating the ORR.

Overall, in the most of cited above experimental studies, the Au/Pt system retains Pt activity up to 20–30% of Au on the surface. The simulations of Pt–Au nanoparticles describing the interplay of Au concentration on the surface and the number of exposed active Pt sites show comparable results. However, the present experimental results reveal quite poor ORR activity of the Pt–Au catalyst with already 20% of Au. This inconsistency is probably associated with the different nature of the studied systems. Since we deal with bimetallic Pt–Au alloys, in addition to the ensemble effect (dilution of Pt atoms on the surface by Au atoms), one should also consider co-existing geometric and ligand effects given by the presence of Au in bulk,⁴⁸ which are confirmed above by XRD and SRPES results.

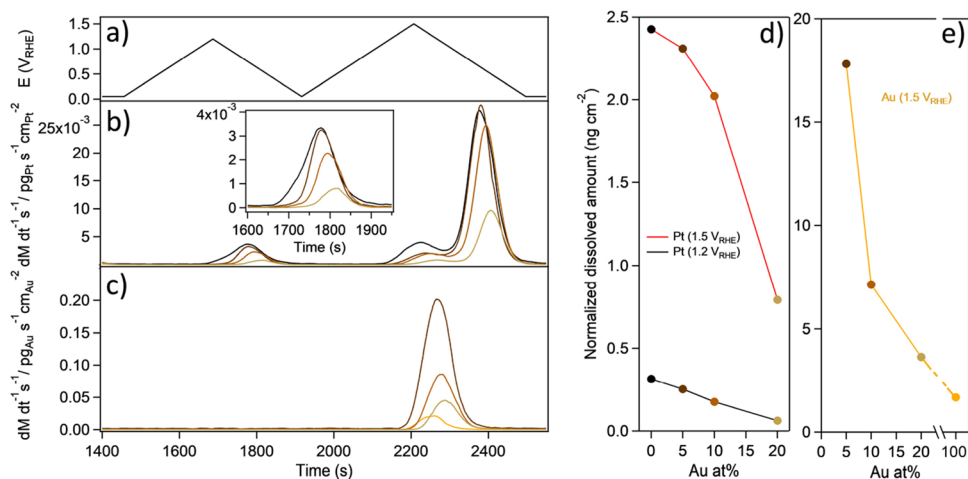


Figure 5. (a) Applied potential program; representative platinum (b) and gold (c) dissolution mass spectrogram taken from Pt–Au alloy catalysts as well as monometallic Pt and Au electrodes; normalized platinum (d) and gold (e) dissolution amounts obtained by the integration of the corresponding mass spectrogram shown in b and c normalized to the concentration of Pt and Au on the surface of Pt–Au alloys.

Both increase with Au content and, because of the detrimental effect on ORR activity in terms of oxygen adsorption energy,^{2,25,26} lower composition–activity threshold in the case of Pt–Au bulk alloys. This assumption is also confirmed in Figure S2c where the kinetic current is compared to the one normalized to the Pt area, since it can be clearly observed that even taking into account the actual Pt area on the surface, the kinetic current is still much lower for PtAu20 in comparison to the other alloys.

An electrochemical flow cell combined with ICP-MS was applied to probe the influence of Au on Pt dissolution. In order to resolve anodic and cathodic dissolution, slow scan rate (5 mV s^{-1}) CVs were acquired from $0.05 V_{\text{RHE}}$ to different upper potentials. Pt dissolution was investigated over an extended potential range, modeling different operational regimes of a PEMFC. Two upper potential limits (UPL) have been employed, 1.2 and $1.5 V_{\text{RHE}}$. At $1.2 V_{\text{RHE}}$, only Pt dissolution occurs, while at $1.5 V_{\text{RHE}}$, both Pt and Au dissolve. Note that we did not use $1.0 V_{\text{RHE}}$ UPL because the dissolution at this potential is below the detection limit of the ICP-MS, which is approximately $3 \text{ pg cm}^{-2} \text{ s}^{-1}$.⁶ However, taking into account previous work on Pt@Au core-shell nanoparticles where the effect of Au on stabilization of Pt dissolution was observed in the range from 1 to $1.2 V_{\text{RHE}}$, we believe that our results can be also extrapolated to lower upper potentials.²² The Pt and Au dissolution profiles for all Pt–Au alloys under study, together with monometallic Pt and Au, are shown in Figure 5b,c. These profiles have been normalized to the corresponding ratio of Pt and Au, as determined from the CO stripping voltammograms shown in Figure 3c. At a UPL of $1.2 V_{\text{RHE}}$, it is difficult to clearly differentiate between anodic and cathodic Pt dissolution (see Figure 5b). However, a clear shoulder appears on the left side for monometallic Pt highlighted in the inset of Figure 5b, which could be deconvoluted as an anodic dissolution peak (see Figure S3). This shoulder, however, vanishes for the Pt–Au samples, evidencing that the anodic dissolution is suppressed by Au. Concerning the cathodic dissolution peak, it can be inferred that the dissolution rate decreases with the increasing Au content. Moreover, the onset of Pt dissolution is shifted to more positive potential values. These observations indicate that Pt stability is improved as the Au content is increased. This trend can be observed from the integrated

dissolved amounts shown in Figure 5d, in which less total normalized dissolution is observed as the Au content increases, being 20, 45, and 80% lower for PtAu5, PtAu10, and PtAu20 samples, respectively, than for monometallic Pt.

At the UPL $1.5 V_{\text{RHE}}$, both Pt and Au dissolve, and anodic and cathodic dissolution for Pt can be clearly resolved in agreement with previous studies.^{16,21} A similar dissolution behavior is pointed out for UPL $1.2 V_{\text{RHE}}$. Both anodic and cathodic dissolution peaks decrease with increasing Au content and shift to more positive potential values. Here, however, the anodic peak does not disappear completely. The ratio between the anodic and cathodic peaks for Pt dissolution was further analyzed. As can be seen in Figure S4, a value near 20% is obtained for pure Pt, while it decreases to around 10% for all Pt–Au samples. It was confirmed in a previous study with 0.25 ML Pt coverage on gold that anodic dissolution is proportional to the coverage of Pt while cathodic dissolution is coverage-independent since the ratio between anodic and cathodic dissolution was reduced four times when compared to pure Pt.²¹ There, it was concluded that Au does not have a noticeable stabilizing effect. However, in the present work, for the PtAu20 sample, with 1.25 times less surface Pt than in the monometallic sample, the ratio between anodic and cathodic dissolution is reduced 2 times compared to pure Pt, giving extra evidence of the stabilizing effect of Au in the studied conditions. Overall, the integrated dissolved amounts of Pt at $1.5 V_{\text{RHE}}$ shown in Figure 5d reveal 10, 20, and 65% lower Pt dissolution for PtAu5, PtAu10, and PtAu20 catalysts, respectively, compared to monometallic Pt.

In the case of Au dissolution, the normalized dissolved amount is higher for the sample with lower Au content and diminishes as the Au content is increased, being the lowest for pure Au. In addition, it can be seen that the onset potential for Au dissolution for PtAu20 is higher than that for pure Au, indicating an alloy behavior in the present samples. A stabilization effect of Pt on Au was also suggested in the previous model study with sub-monolayer Pt on Au, since the amount of dissolved Au after some degradation cycles remained constant although Au coverage increased, and this was ascribed to alloying during this process.²¹

One of the key parameters affecting the leaching of Pt atoms is its binding strength in various kinds of surface positions in

the particles under scrutiny. Obviously, lower-coordinated surface Pt atoms (in corner, edge, step-edge, etc. positions) are more prone to detachment than the higher-coordinated atoms located in the sites of compact surface terraces, e.g., in the (111) nanofacets, which was shown to be the most stable Pt facet.^{10,49,50} The present DFT calculations of Pt₄₀₄ nanoparticles with one Pt atom withdrawn from various surface positions of the pristine Pt₄₀₅ model (see the [Computational Modeling section](#)) estimate that the inner (111) terrace Pt atoms are by almost 1 eV more stable than Pt corner atoms and by 0.6–0.9 eV more stable than other surface Pt atoms residing outside the (111) terraces. The absence of low-coordinated surface Pt atoms (or their decreased number) due to “blocking” such sites by occupying them with Au atoms of the more inert metal makes Pt–Au nanoparticles less prone to disintegration due to Pt leaching and dissolution compared with bare Pt nanoparticles abundantly exposing low-coordinated Pt atoms.

As indicated by the models in [Figure 4](#), Au atoms on the surface start occupying preferentially corners and edges, thereby decreasing the number of less stable low-coordinated Pt atoms and thus decreasing the amount of dissolved platinum. According to the calculated equilibrium chemical ordering with increasing Au content, Au atoms in the skin layer will continuously fill corner and edge positions up to PtAu₃₀ (Pt₁₂₉₁Au₁₇₂ model), where there are already no corner or edge Pt atoms at all on the particle surface. It has to be re-iterated that the discussed above results of computer simulations employing simple regular models of Pt–Au nanoparticles cannot pretend to be quantitative, but they agree with the general picture of the experimentally derived Au content relation with the stability and activity of Pt–Au ORR catalysts.

It can be seen from the ICP-MS results as well as theoretical calculations that the stability increases progressively with Au content in the studied range because of the substitution of Pt atoms by Au on the edges of the nanoparticles, which is in agreement with the literature.²² However, it is essential to juxtapose stability and ORR activity in order to extract conclusions about the optimal Pt–Au composition in terms of both. The ORR results show that while the activity is maintained up to PtAu₁₀, it is unacceptably low already for PtAu₂₀, due to co-existing geometric, ligand, and ensemble effects given by the presence of Au. In light of these results, it can be concluded that PtAu₁₀ is the best composition of the samples under scrutiny, taking into account both ORR activity and stability of the catalysts.

The above results prove that the effectiveness of the Pt–Au alloy for both catalysis and durability is strongly dependent on its composition and structure, indicating the importance of thorough catalyst engineering. Additionally, the systematic study described in this paper can also be used for various promising applications of Pt–Au alloys which expand far beyond fuel cells.^{41,51–54}

CONCLUSIONS

We reported a systematic study of Pt–Au alloys with different compositions (Pt₉₅Au₅, Pt₉₀Au₁₀, and Pt₈₀Au₂₀) prepared using a magnetron sputtering technique. State-of-the-art surface characterization techniques, electrochemistry, and computational modeling were applied to obtain a profound understanding of their composition–structure–activity relationship. A composition threshold was observed within 10–20 at% of Au, beyond which ORR activity dropped significantly. Such

behavior was explained by an interplay of strain, electronic, and ensemble effects caused by platinum alloying with gold.

In parallel, the composition–structure–stability relationship was investigated using SFC combined with ICP-MS to probe Pt dissolution in Pt–Au alloys, which is a fingerprint of ORR catalyst degradation. We showed that Pt dissolution was suppressed by 20, 45, and 80% for PtAu₅, PtAu₁₀, and PtAu₂₀ samples when using upper potential limit 1.2 V_{RHE} and by 10, 20, and 65% when using upper potential limit 1.5 V_{RHE}.

Comparing the obtained results, the Pt–Au alloy with 10% gold represents the most promising composition retaining the activity of monometallic Pt while suppressing Pt dissolution by 50% at the upper potential limit of 1.2 V_{RHE} and 20% at devastating 1.5 V_{RHE}.

ASSOCIATED CONTENT

Supporting Information

The Supporting Information is available free of charge at <https://pubs.acs.org/doi/10.1021/acsami.2c18655>.

EDX and XPS spectra of Pt–Au alloys; kinetic analysis of the ORR results; and additional analysis of dissolution profiles (PDF)

AUTHOR INFORMATION

Corresponding Author

Ivan Khalakhan – Faculty of Mathematics and Physics, Department of Surface and Plasma Science, Charles University, Prague 8 18000, Czech Republic; orcid.org/0000-0003-2929-4148; Phone: +420-22191-2321; Email: ivan.khalakhan@mff.cuni.cz, khalakhan@gmail.com; Fax: +420-22191-2297

Authors

Xianxian Xie – Faculty of Mathematics and Physics, Department of Surface and Plasma Science, Charles University, Prague 8 18000, Czech Republic

Valentín Briega-Martos – Forschungszentrum Jülich GmbH, Helmholtz Institute Erlangen-Nürnberg for Renewable Energy (IEK-11), Erlangen 91058, Germany; orcid.org/0000-0001-8407-2260

Riccardo Farris – Departament de Ciència de Materials i Química Física & Institut de Química Teòrica i Computacional (IQTUB), Universitat de Barcelona, Barcelona 08028, Spain; orcid.org/0000-0002-8157-6786

Milan Dopita – Faculty of Mathematics and Physics, Department of Condensed Matter Physics, Charles University, Prague 2 12116, Czech Republic

Mykhailo Vorokhta – Faculty of Mathematics and Physics, Department of Surface and Plasma Science, Charles University, Prague 8 18000, Czech Republic; orcid.org/0000-0001-8382-7027

Tomáš Skála – Faculty of Mathematics and Physics, Department of Surface and Plasma Science, Charles University, Prague 8 18000, Czech Republic; orcid.org/0000-0003-2909-9422

Iva Matolinová – Faculty of Mathematics and Physics, Department of Surface and Plasma Science, Charles University, Prague 8 18000, Czech Republic; orcid.org/0000-0001-6808-7809

Konstantin M. Neyman – Departament de Ciència de Materials i Química Física & Institut de Química Teòrica i

Computacional (IQTUB), Universitat de Barcelona, Barcelona 08028, Spain; ICREA (Institució Catalana de Recerca i Estudis Avançats), Barcelona 08010, Spain; orcid.org/0000-0002-5242-5567

Serhiy Cherevko – Forschungszentrum Jülich GmbH, Helmholtz Institute Erlangen-Nürnberg for Renewable Energy (IEK-11), Erlangen 91058, Germany; orcid.org/0000-0002-7188-4857

Complete contact information is available at: <https://pubs.acs.org/10.1021/acsami.2c18655>

Notes

The authors declare no competing financial interest.

ACKNOWLEDGMENTS

The work was financially supported the Czech Science Foundation, project No. 22-03643S. X.X. and I.M. acknowledge the structural fund project No. CZ.02.1.01/0.0/0.0/16_025/0007414. The authors are also grateful to the CERIC-ERIC consortium for access to the experimental facility and partial financial support. X.X. and I.K. further acknowledge mobility project No. 8J22DE014 provided by the Czech Ministry of Education, Youth and Sports. V.B.-M. and S.C. acknowledge the mobility project No. 57602590 provided by the Deutscher Akademischer Austauschdienst German Academic Exchange Service (DAAD) and Deutsche Forschungsgemeinschaft (DFG) for financial support within the grant CH 1763/5-1. R.F. and K.M.N. gratefully acknowledge support by the Spanish grants MDM-2017-0767 and CEX2021-001202-M (to IQTUB), PGC2018-093863-B-C22, PID2021-128217NB-I00, and PRE2020-091903.

REFERENCES

- (1) The European Commission. A European Green Deal https://ec.europa.eu/info/strategy/priorities-2019-2024/european-green-deal_en.
- (2) Nørskov, J. K.; Rossmeisl, J.; Logadottir, A.; Lindqvist, L.; Kitchin, J. R.; Bligaard, T.; Jónsson, H. Origin of the Overpotential for Oxygen Reduction at a Fuel-Cell Cathode. *J. Phys. Chem. B* **2004**, *108*, 17886–17892.
- (3) Meier, J. C.; Galeano, C.; Katsounaros, I.; Witte, J.; Bongard, H. J.; Topalov, A. A.; Baldizzone, C.; Mezzavilla, S.; Schüth, F.; Mayrhofer, K. J. J. Design Criteria for Stable Pt/C Fuel Cell Catalysts. *Beilstein J. Nanotechnol.* **2014**, *5*, 44–67.
- (4) Bogar, M.; Yakovlev, Y.; Sandbeck, D. J. S.; Cherevko, S.; Matolínová, I.; Amenitsch, H.; Khalakhan, I. Interplay Among Dealloying, Ostwald Ripening, and Coalescence in Pt_xNi_{100-x} Bimetallic Alloys under Fuel-Cell-Related Conditions. *ACS Catal.* **2021**, *11*, 11360–11370.
- (5) Martens, I.; Chattot, R.; Drnec, J. Decoupling Catalyst Aggregation, Ripening, and Coalescence Processes inside Operating Fuel Cells. *J. Power Sources* **2022**, *521*, No. 230851.
- (6) Cherevko, S.; Keeley, G. P.; Geiger, S.; Zeradjanin, A. R.; Hodnik, N.; Kulyk, N.; Mayrhofer, K. J. J. Dissolution of Platinum in the Operational Range of Fuel Cells. *ChemElectroChem* **2015**, *2*, 1471–1478.
- (7) Meier, J. C.; Galeano, C.; Katsounaros, I.; Topalov, A. A.; Kostka, A.; Schüth, F.; Mayrhofer, K. J. J. Degradation Mechanisms of Pt/C Fuel Cell Catalysts under Simulated Start–Stop Conditions. *ACS Catal.* **2012**, *2*, 832–843.
- (8) Guilminot, E.; Corcella, A.; Charlot, F.; Maillard, F.; Chatenet, M. Detection of Pt²⁺ Ions and Pt Nanoparticles Inside the Membrane of a Used PEMFC. *J. Electrochem. Soc.* **2007**, *154*, B96.
- (9) Hodnik, N.; Zorko, M.; Jozinović, B.; Bele, M.; Dražič, G.; Hočevar, S.; Gaberšček, M. Severe Accelerated Degradation of PEMFC Platinum Catalyst: A Thin Film IL-SEM Study. *Electrochem. Commun.* **2013**, *30*, 75–78.
- (10) Lopes, P. P.; Strmcnik, D.; Tripkovic, D.; Connell, J. G.; Stamenkovic, V.; Markovic, N. M. Relationships between Atomic Level Surface Structure and Stability/Activity of Platinum Surface Atoms in Aqueous Environments. *ACS Catal.* **2016**, *6*, 2536–2544.
- (11) Topalov, A. A.; Cherevko, S.; Zeradjanin, A. R.; Meier, J. C.; Katsounaros, I.; Mayrhofer, K. J. J. Towards a Comprehensive Understanding of Platinum Dissolution in Acidic Media. *Chem. Sci.* **2014**, *5*, 631–638.
- (12) Topalov, A. A.; Katsounaros, I.; Auinger, M.; Cherevko, S.; Meier, J. C.; Klemm, S. O.; Mayrhofer, K. J. J. Dissolution of Platinum: Limits for the Deployment of Electrochemical Energy Conversion? *Angew. Chem., Int. Ed.* **2012**, *51*, 12613–12615.
- (13) Cherevko, S.; Topalov, A. A.; Zeradjanin, A. R.; Keeley, G. P.; Mayrhofer, K. J. J. Temperature-Dependent Dissolution of Polycrystalline Platinum in Sulfuric Acid Electrolyte. *Electrocatalysis* **2014**, *5*, 235–240.
- (14) Khalakhan, I.; Bogar, M.; Vorokhta, M.; Kúš, P.; Yakovlev, Y.; Dopita, M.; Sandbeck, D. J. S.; Cherevko, S.; Matolínová, I.; Amenitsch, H. Evolution of the PtNi Bimetallic Alloy Fuel Cell Catalyst under Simulated Operational Conditions. *ACS Appl. Mater. Interfaces* **2020**, *12*, 17602–17610.
- (15) Šala, M.; Gaberšček, M.; Pavlišič, A.; Hodnik, N.; Jovanovič, P.; Šelih, V. S. Platinum Dissolution and Redeposition from Pt/C Fuel Cell Electrocatalyst at Potential Cycling. *J. Electrochem. Soc.* **2018**, *165*, F3161–F3165.
- (16) Cherevko, S.; Zeradjanin, A. R.; Keeley, G. P.; Mayrhofer, K. J. J. A Comparative Study on Gold and Platinum Dissolution in Acidic and Alkaline Media. *J. Electrochem. Soc.* **2014**, *161*, H822–H830.
- (17) Singh, K.; Tetteh, E. B.; Lee, H.-Y.; Kang, T.-H.; Yu, J.-S. Tailor-Made Pt Catalysts with Improved Oxygen Reduction Reaction Stability/Durability. *ACS Catal.* **2019**, *9*, 8622–8645.
- (18) Ji, S. G.; Kwon, H. C.; Kim, T.-H.; Sim, U.; Choi, C. H. Does the Encapsulation Strategy of Pt Nanoparticles with Carbon Layers Really Ensure Both Highly Active and Durable Electrocatalysis in Fuel Cells? *ACS Catal.* **2022**, *12*, 7317–7325.
- (19) Karuppanan, M.; Kim, Y.; Gok, S.; Lee, E.; Hwang, J. Y.; Jang, J.-H.; Cho, Y.-H.; Lim, T.; Sung, Y.-E.; Kwon, O. J. A Highly Durable Carbon-Nanofiber-Supported Pt–C Core–shell Cathode Catalyst for Ultra-Low Pt Loading Proton Exchange Membrane Fuel Cells: Facile Carbon Encapsulation. *Energy Environ. Sci.* **2019**, *12*, 2820–2829.
- (20) Gatalo, M.; Jovanovič, P.; Polymeros, G.; Grote, J.-P.; Pavlišič, A.; Ruiz-Zepeda, F.; Šelih, V. S.; Šala, M.; Hočevar, S.; Bele, M.; et al. Positive Effect of Surface Doping with Au on the Stability of Pt-Based Electrocatalysts. *ACS Catal.* **2016**, *6*, 1630–1634.
- (21) Cherevko, S.; Keeley, G. P.; Kulyk, N.; Mayrhofer, K. J. J. Pt Sub-Monolayer on Au: System Stability and Insights into Platinum Electrochemical Dissolution. *J. Electrochem. Soc.* **2016**, *163*, H228–H233.
- (22) Lopes, P. P.; Li, D.; Lv, H.; Wang, C.; Tripkovic, D.; Zhu, Y.; Schimmenti, R.; Daimon, H.; Kang, Y.; Snyder, J.; et al. Eliminating Dissolution of Platinum-Based Electrocatalysts at the Atomic Scale. *Nat. Mater.* **2020**, *19*, 1207–1214.
- (23) Zhang, J.; Sasaki, K.; Sutter, E.; Adzic, R. R. Stabilization of Platinum Oxygen-Reduction Electrocatalysts Using Gold Clusters. *Science* **2007**, *315*, 220–222.
- (24) Takahashi, S.; Chiba, H.; Kato, T.; Endo, S.; Hayashi, T.; Todoroki, N.; Wadayama, T. Oxygen Reduction Reaction Activity and Structural Stability of Pt–Au Nanoparticles Prepared by Arc-Plasma Deposition. *Phys. Chem. Chem. Phys.* **2015**, *17*, 18638–18644.
- (25) Yin, S.; Ding, Y. Bimetallic PtAu Electrocatalysts for the Oxygen Reduction Reaction: Challenges and Opportunities. *Dalton Trans.* **2020**, *49*, 4189–4199.
- (26) Luo, J.; Maye, M. M.; Petkov, V.; Kariuki, N. N.; Wang, L.; Njoki, P.; Mott, D.; Lin, Y.; Zhong, C.-J. Phase Properties of Carbon-Supported Gold–Platinum Nanoparticles with Different Bimetallic Compositions. *Chem. Mater.* **2005**, *17*, 3086–3091.

- (27) Schuppert, A. K.; Topalov, A. A.; Katsounaros, I.; Klemm, S. O.; Mayrhofer, K. J. J. A Scanning Flow Cell System for Fully Automated Screening of Electrocatalyst Materials. *J. Electrochem. Soc.* **2012**, *159*, F670–F675.
- (28) Kozlov, S. M.; Kovács, G.; Ferrando, R.; Neyman, K. M. How to Determine Accurate Chemical Ordering in Several Nanometer Large Bimetallic Crystallites from Electronic Structure Calculations. *Chem. Sci.* **2015**, *6*, 3868–3880.
- (29) Kovács, G.; Kozlov, S. M.; Neyman, K. M. Versatile Optimization of Chemical Ordering in Bimetallic Nanoparticles. *J. Phys. Chem. C* **2017**, *121*, 10803–10808.
- (30) Vega, L.; Aleksandrov, H. A.; Farris, R.; Bruix, A.; Viñes, F.; Neyman, K. M. Chemical Ordering in Pt–Au, Pt–Ag and Pt–Cu Nanoparticles from Density Functional Calculations Using a Topological Approach. *Mater. Adv.* **2021**, *2*, 6589–6602.
- (31) Danielis, N.; Vega, L.; Fronzoni, G.; Stener, M.; Bruix, A.; Neyman, K. M. AgPd, AuPd, and AuPt Nanoalloys with Ag- or Au-Rich Compositions: Modeling Chemical Ordering and Optical Properties. *J. Phys. Chem. C* **2021**, *125*, 17372–17384.
- (32) Khalakhan, I.; Choukourou, A.; Vorokhta, M.; Kůš, P.; Matolínová, I.; Matolín, V. In Situ Electrochemical AFM Monitoring of the Potential-Dependent Deterioration of Platinum Catalyst during Potentiodynamic Cycling. *Ultramicroscopy* **2018**, *187*, 64–70.
- (33) Irissou, E.; Laplante, F.; Garbarino, S.; Chaker, M.; Guay, D. Structural and Electrochemical Characterization of Metastable PtAu Bulk and Surface Alloys Prepared by Crossed-Beam Pulsed Laser Deposition. *J. Phys. Chem. C* **2010**, *114*, 2192–2199.
- (34) Petkov, V.; Wanjala, B. N.; Loukrakpam, R.; Luo, J.; Yang, L.; Zhong, C.-J.; Shastri, S. Pt–Au Alloying at the Nanoscale. *Nano Lett.* **2012**, *12*, 4289–4299.
- (35) Khalakhan, I.; Vorokhta, M.; Xie, X.; Piliai, L.; Matolínová, I. On the Interpretation of X-Ray Photoelectron Spectra of Pt–Cu Bimetallic Alloys. *J. Electron Spectrosc. Relat. Phenomena* **2021**, *246*, No. 147027.
- (36) Khalakhan, I.; Vorokhta, M.; Václavů, M.; Šmíd, B.; Lavková, J.; Matolínová, I.; Fiala, R.; Tsud, N.; Skála, T.; Matolín, V. In-Situ Electrochemical Atomic Force Microscopy Study of Aging of Magnetron Sputtered Pt–Co Nanoalloy Thin Films during Accelerated Degradation Test. *Electrochim. Acta* **2016**, *211*, 52–58.
- (37) Prieto, M. J.; Carbonio, E. A.; Landers, R.; de Siervo, A. Promotion Effect of Platinum on Gold's Reactivity: A High-Resolution Photoelectron Spectroscopy Study. *J. Phys. Chem. C* **2016**, *120*, 10227–10236.
- (38) Heimann, P.; van der Veen, J. F.; Eastman, D. E. Structure-Dependent Surface Core Level Shifts for the Au(111), (100), and (110) Surfaces. *Solid State Commun.* **1981**, *38*, 595–598.
- (39) Wang, D.; Cui, X.; Xiao, Q.; Hu, Y.; Wang, Z.; Yiu, Y. M.; Sham, T. K. Electronic Behaviour of Au–Pt Alloys and the 4f Binding Energy Shift Anomaly in Au Bimetallics- X-Ray Spectroscopy Studies. *AIP Adv.* **2018**, *8*, 65210.
- (40) Ren, F.; Zhai, C.; Zhu, M.; Wang, C.; Wang, H.; Bin, D.; Guo, J.; Yang, P.; Du, Y. Facile Synthesis of PtAu Nanoparticles Supported on Polydopamine Reduced and Modified Graphene Oxide as a Highly Active Catalyst for Methanol Oxidation. *Electrochim. Acta* **2015**, *153*, 175–183.
- (41) Duchesne, P. N.; Li, Z. Y.; Deming, C. P.; Fung, V.; Zhao, X.; Yuan, J.; Regier, T.; Aldalbahi, A.; Almarhoon, Z.; Chen, S.; et al. Golden Single-Atomic-Site Platinum Electrocatalysts. *Nat. Mater.* **2018**, *17*, 1033–1039.
- (42) Yang, S.; Lee, H. Atomically Dispersed Platinum on Gold Nano-Octahedra with High Catalytic Activity on Formic Acid Oxidation. *ACS Catal.* **2013**, *3*, 437–443.
- (43) Kumar, S.; Zou, S. Electrooxidation of Carbon Monoxide and Methanol on Platinum-Overlayer-Coated Gold Nanoparticles: Effects of Film Thickness. *Langmuir* **2007**, *23*, 7365–7371.
- (44) Briega-Martos, V.; Herrero, E.; Feliu, J. M. Effect of PH and Water Structure on the Oxygen Reduction Reaction on Platinum Electrodes. *Electrochim. Acta* **2017**, *241*, 497–509.
- (45) Gómez-Marín, A.; Feliu, J.; Edson, T. Reaction Mechanism for Oxygen Reduction on Platinum: Existence of a Fast Initial Chemical Step and a Soluble Species Different from H₂O₂. *ACS Catal.* **2018**, *8*, 7931–7943.
- (46) Escudero-Escribano, M.; Malacrida, P.; Hansen, M. H.; Vej-Hansen, U. G.; Velázquez-Palenzuela, A.; Tripkovic, V.; Schiøtz, J.; Rossmeisl, J.; Stephens, I. E. L.; Chorkendorff, I. Tuning the Activity of Pt Alloy Electrocatalysts by Means of the Lanthanide Contraction. *Science* **2016**, *352*, 73–76.
- (47) Lindahl, N.; Zamburlini, E.; Feng, L.; Grönbeck, H.; Escudero-Escribano, M.; Stephens, I. E. L.; Chorkendorff, I.; Langhammer, C.; Wickman, B. High Specific and Mass Activity for the Oxygen Reduction Reaction for Thin Film Catalysts of Sputtered Pt₃Y. *Adv. Mater. Interfaces* **2017**, *4*, No. 1700311.
- (48) Deng, Y.-J.; Tripkovic, V.; Rossmeisl, J.; Arenz, M. Oxygen Reduction Reaction on Pt Overlayers Deposited onto a Gold Film: Ligand, Strain, and Ensemble Effect. *ACS Catal.* **2016**, *6*, 671–676.
- (49) Fuchs, T.; Drnec, J.; Calle-Vallejo, F.; Stubbs, N.; Sandbeck, D. J. S.; Ruge, M.; Cherevko, S.; Harrington, D. A.; Magnussen, O. M. Structure Dependency of the Atomic-Scale Mechanisms of Platinum Electro-Oxidation and Dissolution. *Nat. Catal.* **2020**, *3*, 754–761.
- (50) Sandbeck, D. J. S.; Brummel, O.; Mayrhofer, K. J. J.; Libuda, J.; Katsounaros, I.; Cherevko, S. Dissolution of Platinum Single Crystals in Acidic Medium. *ChemPhysChem* **2019**, *20*, 2997–3003.
- (51) Guan, Q.; Zhu, C.; Lin, Y.; Vovk, E. I.; Zhou, X.; Yang, Y.; Yu, H.; Cao, L.; Wang, H.; Zhang, X.; et al. Bimetallic Monolayer Catalyst Breaks the Activity–selectivity Trade-off on Metal Particle Size for Efficient Chemoselective Hydrogenations. *Nat. Catal.* **2021**, *4*, 840–849.
- (52) Krstajić Pajić, M. N.; Stevanović, S. I.; Radmilović, V. V.; Gavrilović-Wohlmuther, A.; Zabinski, P.; Elezović, N. R.; Radmilović, V. R.; Gojković, S. L.; Jovanović, V. M. Dispersion Effect in Formic Acid Oxidation on PtAu/C Nanocatalyst Prepared by Water-in-Oil Microemulsion Method. *Appl. Catal. B Environ.* **2019**, *243*, 585–593.
- (53) Wang, J.; Gao, H.; Sun, F.; Xu, C. Nanoporous PtAu Alloy as an Electrochemical Sensor for Glucose and Hydrogen Peroxide. *Sens. Actuators B Chem.* **2014**, *191*, 612–618.
- (54) Yin, M.; Huang, Y.; Liang, L.; Liao, J.; Liu, C.; Xing, W. Inhibiting CO Formation by Adjusting Surface Composition in PtAu Alloys for Methanol Electrooxidation. *Chem. Commun.* **2011**, *47*, 8172–8174.